

Understanding the thermal properties of amorphous solids using machine-learning-based interatomic potentials

Gabriele C. Sosso, Volker L. Deringer, Stephen R. Elliott & Gábor Csányi

To cite this article: Gabriele C. Sosso, Volker L. Deringer, Stephen R. Elliott & Gábor Csányi (2018): Understanding the thermal properties of amorphous solids using machine-learning-based interatomic potentials, Molecular Simulation, DOI: [10.1080/08927022.2018.1447107](https://doi.org/10.1080/08927022.2018.1447107)

To link to this article: <https://doi.org/10.1080/08927022.2018.1447107>



Published online: 13 Mar 2018.



Submit your article to this journal [↗](#)



Article views: 68



View related articles [↗](#)



View Crossmark data [↗](#)



Understanding the thermal properties of amorphous solids using machine-learning-based interatomic potentials

Gabriele C. Sosso^a , Volker L. Deringer^{b,c} , Stephen R. Elliott^c and Gábor Csányi^b 

^aDepartment of Chemistry and Centre for Scientific Computing, University of Warwick, Coventry, UK; ^bDepartment of Engineering, University of Cambridge, Cambridge, UK; ^cDepartment of Chemistry, University of Cambridge, Cambridge, UK

ABSTRACT

Understanding the thermal properties of disordered systems is of fundamental importance for condensed matter physics - and for practical applications as well. While quantities such as the thermal conductivity are usually well characterised experimentally, their microscopic origin is often largely unknown - hence the pressing need for molecular simulations. However, the time and length scales involved with thermal transport phenomena are typically well beyond the reach of *ab initio* calculations. On the other hand, many amorphous materials are characterised by a complex structure, which prevents the construction of classical interatomic potentials. One way to get past this deadlock is to harness machine-learning (ML) algorithms to build interatomic potentials: these can be nearly as computationally efficient as classical force fields while retaining much of the accuracy of first-principles calculations. Here, we discuss neural network potentials (NNPs) and Gaussian approximation potentials (GAPs), two popular ML frameworks. We review the work that has been devoted to investigate, via NNPs, the thermal properties of phase-change materials, systems widely used in non-volatile memories. In addition, we present recent results on the vibrational properties of amorphous carbon, studied via GAPs. In light of these results, we argue that ML-based potentials are among the best options available to further our understanding of the vibrational and thermal properties of complex amorphous solids.

ARTICLE HISTORY

Received 14 November 2017
Accepted 22 February 2018

KEYWORDS

Neural networks; Gaussian approximation potential (GAP) models; thermal conductivity; phase-change materials; amorphous carbon

1. Introduction

The thermal properties of disordered solids are a problem of great interest in solid-state physics and materials science [1–6]. Many quantities of practical relevance, such as the thermal conductivity of a material, are largely determined by the underlying vibrational properties [7–9]. In crystals, which exhibit periodic long-range order, the vibrational excitations are likewise periodic and described by quantised lattice vibrational modes, so-called phonons [10,11]. In amorphous systems, the absence of long-range order leads to a coexistence of localised vibrations and propagating, plane wave-like modes. This poses a significant challenge for molecular simulations, as large structural models (typically containing between one thousand and a million atoms) are needed to avoid imposing an artificial length scale on the structural and vibrational properties of the system [12,13]. In fact, any atomistic simulation of *amorphous* matter must be performed in a simulation box with periodic boundary conditions that does have translational symmetry. In addition, we shall see that different computational techniques may be necessary to investigate, say, the different mechanisms of heat conduction in complex disordered systems.

According to the labelling introduced by Allen and Feldman (AF) [14], the entirety of vibrational modes ('vibrons') in amorphous solids consist of localised and extended vibrations ('locons' and 'extendons', respectively). The latter can be further labelled as 'propagons' or 'diffusons' according to whether or not their wavenumber ω is lower (propagons) or higher (diffusons) than the so-called Ioffe-Regel crossover frequency ω_{co} , for which

their mean-free path is comparable to the wavelength [15]. This is illustrated in Figure 1 for the prototypical example of amorphous silicon (*a*-Si). *a*-Si can be considered as a relatively 'simple' amorphous solid, in that its structure can be approximated solely in terms of tetrahedral units (Figure 1(a)) [16]. And yet, even this prototypical amorphous solid shows a complex vibrational landscape. Figure 1(b) illustrates how the *a*-Si vibrational density of states (VDOS) originates from contributions by different types of vibrons. It is also worth noting that the AF framework applies to (quasi)harmonic solids, thus neglecting the contribution of non-harmonic motions, usually described by two-level states [17,18]. While the latter usually play very little role in determining, e.g. the thermal conductivity at room temperature, their mention should help to emphasise the sheer complexity of the vibrational landscape of disordered systems (as compared to crystals).

Vibrational properties of amorphous solids, with their admittedly complicated taxonomy, are by far not just of academic interest: they have direct impact on real-life applications. Window glasses are one familiar example: their thermal expansion, thermal-shock resistance and thermal conductivity are all intimately connected with their atomic-level structure [20–22], and thus with their vibrational properties. Another important example is given by glassy Li-ion batteries, where the electronic contribution to the thermal conductivity is often non-negligible, and the thermal stability of the material heavily influences device performance [23–27]. How heat is conducted and dissipated through an amorphous matrix is also of great relevance in the

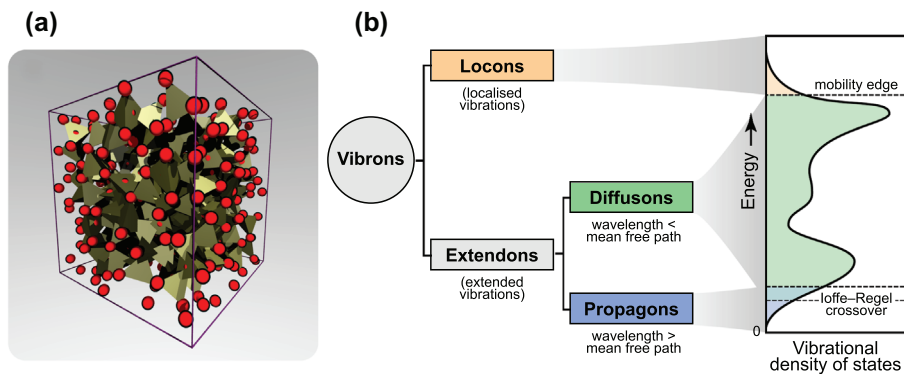


Figure 1. (Colour online) (a) A 512-atom structural model of amorphous silicon (*a*-Si), taken from Ref. [19]. The tetrahedrality of the network of silicon atoms (red spheres) is highlighted via the coordination polyhedra. (b) Taxonomy of vibrations in glasses and their contributions to the vibrational density of states (VDOS; this sketch is based on Ref. [14]), illustrated for the prototypical case of *a*-Si.

context of data storage, as the new generations of non-volatile memories based on phase-change processes deal with active volumes only a few nanometres switched by voltage-induced heat pulses [28,30,31]; we will re-visit this exciting class of materials below. Thus, there is a need to better understand the vibrational and thermal properties in nanostructures and nanoconfined environments.

Molecular simulations offer a unique opportunity to obtain microscopic insight into the origin of thermal properties – including disordered systems. This is of clear technological interest, as there are ways to alter, say, the thermal conductivity of a given solid, by tuning the extent of disorder (via doping, or intercalation, or nanostructuring) [32]. Computational investigations can thus contribute to connect the molecular-level details of materials with macroscopic functional properties, complementing and guiding experiments and applications.

In principle, *ab initio* simulations (typically based on Density Functional Theory, DFT [33]) would be the tool of the trade to compute properties such as the electronic contribution to the thermal conductivity or, as we shall see in Section 3.2, the thermal boundary resistance at interfaces. Unfortunately, the computational requirements to compute properties such as the thermal conductivity are often well beyond the reach of *ab initio* calculations. For instance, estimating the thermal conductivity for the phase-change material GeTe (Section 3.1.1) required a 4096-atom model and a molecular-dynamics (MD) simulation on a nanosecond timescale. This MD run involved millions of individual time steps, at each of which the forces on atoms need to be evaluated [34] – it becomes immediately clear why this is not feasible with DFT, which requires very significant effort to converge the wave function of even one single 4096-atom snapshot. Thus, one is typically forced to resort to classical MD, which however poses yet another major issue: that of the availability and accuracy of parametrised force fields. For simple systems, fairly accurate force fields are typically available [35–40]. The same holds for a number of covalent glasses such as silica, for which a number of viable options do exist [41–43]; furthermore, empirical potentials can be significantly improved by physically and chemically motivated modifications, such as environment-dependent cutoff radii [44]. However, the situation is dramatically different when dealing with more

complex materials: multicomponent alloys, Li-ion conducting glasses and chalcogenide glasses for electronic applications are all typically characterised by diverse local atomic environments and varying degrees of disorder – including extended structural defects. Crafting accurate interatomic potentials for such systems is a formidable challenge, one that has been worrying materials scientists for decades.

One way to harness the computational efficiency of classical MD while retaining a good deal of the accuracy of *ab initio* simulations is to take advantage of machine learning (ML). These are exciting times for the ML community, as these algorithms are quickly spreading through an impressive number of disciplines and technologies [45–48]. In the context of molecular simulations, ML algorithms are used as particularly clever fitting tools to obtain interatomic potentials, starting from data-sets of configurations and (typically) energies computed *ab initio* [49]. We shall see that this opens a wealth of possibilities, including an unprecedented opportunity to study thermal properties of complex amorphous solids by means of molecular simulations.

In this Review, we highlight emerging applications of ML-based interatomic potentials (MLIPs) to investigate vibrational and thermal properties of amorphous solids. In particular, we focus on the prototypical phase-change material GeTe, which is of relevance for non-volatile memory applications. We shall see that MLIPs allow not only to compute properties such as thermal conductivity and thermal boundary resistance, but also to cross-validate results from different computational techniques. We also take a quick survey of amorphous carbon, a structurally quite surprisingly complex system for which an MLIP has recently been constructed. We discuss the need for these sort of potentials, their limitations and their unique importance in helping us understanding the microscopic subtleties that rule thermal transport in disordered systems. It is worth noting at this stage that ML algorithms have also been used to predict the thermal properties of materials *based on large experimental datasets* [50,51]. This is a fascinating topic but has little in common with the construction of interatomic potentials – as such, it will not be covered in this work.

The content is organised as follows: we start in Section 2 by introducing ML-based interatomic potentials, focusing on two approaches relevant for our own work, viz. Neural Network

Potentials (NNPs) and Gaussian Approximation Potentials (GAPs) be used. While the choice of input structures is by far not trivial, In Section 3, we review the body of work devoted to unravelling, by means of a NNP, the thermal properties of the phase-change material GeTe. Particular emphasis will be on the thermal conductivity and the thermal boundary resistance. In Section 4, we present recent work based on a GAP for amorphous carbon and explore future directions. In Section 5, we argue that MLIPs can constitute the way forward to tackle molecular simulations of thermal properties of complex amorphous solids. We also address the limitations of MLIPs when it comes to dealing with high levels of material complexity.

2. Machine learning for atomistic simulations: why and how

The thermal properties of amorphous solids are an excellent example of a challenges for molecular simulations. In this case, accuracy is crucial just as much as computational efficiency: the former, to treat the subtleties of the vibrational landscape; the latter, to enable simulations on large length/long time scales (nm and ns respectively). Accuracy is usually associated with first-principles (*ab initio*) calculations, computational efficiency with classical molecular dynamics. The question, now, is *how to get the best of both worlds?* ML-based methods offer a solution, and as such they have been attracting ever-growing interest over recent years [52–62].

Let us start with a word of caution. ‘Machine learning’ as such is doubtlessly a trending concept, far beyond fundamental research: these days, the general public is perfectly aware, if not of what ML is exactly, surely of what we use it for. Pattern recognition is a popular example [63], together with data analysis [64–66], web search engines and personal assistants, not to mention the celebrated victory of AlphaGo against a human player [67]. However, for the purpose of constructing interatomic potentials, ML algorithms are little more or little less than fairly clever fitting tools. A more detailed review discussing MLIPs can be found, e.g. in Ref. [49]; we here limit ourselves to the basic principles.

MLIPs perform a high-dimensional fit to a given potential-energy surface (PES), and therefore, the starting point is to build a database containing roughly 10^2 – 10^4 small configurations (each containing maybe a hundred atoms or molecules), for which it is feasible to compute energies and forces *ab initio*. Once this database has been created, the connection between atomic structure and potential energy has to be encoded in a suitable form to be fed into the ML algorithm. This requires so-called *descriptors*, mathematical objects that obey certain requisites and represent the local atomic environments (LAEs): imagine sitting on a particular atom and trying to describe everything you see up to a certain cutoff radius (but no further). Once the descriptors have been settled, the ML algorithm feeds upon the information in the database and interpolates, for any arbitrary LAE, its contribution to the potential energy of the system. At this stage, one can hence calculate energies (and, importantly, forces) for any number of LAEs – that is, one can treat even very large systems with trivially linear scaling behaviour.

The construction of the *ab initio* database is largely independent from which particular ML method and descriptors are to

and crucial for the success of any MLIP, creating the database ultimately requires a huge number of *ab initio* simulations. The shape and the properties of the descriptors have to be consistent with the core of the particular ML approach. While multiple options do exist that can be used with the same ML algorithm, the descriptors can substantially differ from one implementation to another. Similarly, a rather diverse array of algorithms exist, using artificial neural networks, Gaussian processes, etc. – so different MLIP architectures employ very different recipes. As such, these potentials cannot be easily used across different ML implementations. Importantly, though, the *ab initio* data could in principle be shared.

2.1. Implementations: neural-network potentials and gaussian approximation potentials

A growing number of algorithmic frameworks exist to construct MLIPs; the interested reader is referred to a detailed overview given by Behler [49] as well as several very recent examples that are beyond the scope of this work [68–70]. Here, we shall only consider two arguably successfully used approaches that we have employed in our own research: namely, artificial neural-network potentials as well as Gaussian approximation potentials. We do not aim to recommend one over the other – both are useful, and different, approaches towards a similar problem.

NNPs take advantage of feed-forward neural networks to construct a PES starting from the energies of the configurations in the reference database. They provide an analytic representation of the PES, so that computing the forces acting on each atom in the system (which is the basis of MD simulations) is simply a matter of taking the derivative with respect to the atomic positions. The central approximation of NNPs is that the total energy E of a system can be decomposed into a sum of individual contributions ε_i ,

$$E_{\text{total}} = \sum_i \varepsilon_i, \quad (1)$$

where each of these *atomic energies* is a function of the LAE of the i -th atom, and the latter is in turn defined using a set of descriptors. NNPs typically employ combinations of so-called Atom-centred Symmetry Functions (ACSFs) for this task [71]: these functions take into account the distances and angles between pairs and triplets of atoms, respectively, and their combination results in a multi-body description of an LAE.

Note that the above expression assumes *locality* (‘short-sightedness’); that is, it assumes that the energetics and forces of a given atom depend *only* on its immediate environment as specified by a cutoff radius. The latter typically encompasses the first and second coordination shells, leading to cutoff radii of the order of 5–10 Å. This approximation applies to GAPs as well, and it is valid for many covalently bonded and metallic materials, while it faces challenges when long-range (ionic and/or dispersion) interactions are present. The latter can implicitly be taken into account by producing a data-set with dispersion-corrected/included exchange-correlation functionals. The assumption is that the contributions of such long-range forces lead structural modifications of the systems which can be described

within the framework of LAEs – which may or may not be an accurate assumption. In some cases, even a ‘standard’ DFT methodology may lead to a reasonable description: for example, the Local Density Approximation (LDA) functional gives an acceptable value for the inter-layer distance in graphite (one of the reasons it was chosen for the carbon potential described below), whereas standard GGA functionals will fail at this task [72,73]. Care must be taken in choosing the underlying computational method, as always. The situation is much more complex when dealing with charged systems, where electrostatic interactions play a central role. In that case, charges have to be taken into account. In the case of NNPs, this is done by introducing a dedicated set of neural networks dealing exclusively with the electrostatics. This approach has been successful in e.g. obtaining a NNP for zinc oxide [74].

In the GAP framework, the total energy is likewise decomposed into a sum of individual contributions ε_i , dependent on the LAE of the central atom. In this case, the LAE is encoded by a so-called ‘descriptor vector’, which we denote by \vec{q}_i . The choice of these vectors is arbitrary in the first instance, and depends on the problem at hand. A simple descriptor for a diatomic molecule could be the (scalar) distance between the two atoms. For more complex atomistic systems, in particular for condensed-phase materials, the recently introduced Smooth Overlap of Atomic Positions (SOAP) framework [75] has proved successful. Let us assume again that the total energy is a sum of local energies (Equation (1)), and that the latter are expressed in terms of some arbitrary and (possibly) unknown basis functions $\{\phi_t\}$, combined using linear combination coefficients, α_t .

$$\varepsilon_i(\vec{q}_i) = \sum_t \alpha_t \phi_t(\vec{q}_i) \equiv \varepsilon_i(\vec{\alpha}, \vec{q}_i) \quad (2)$$

These coefficients are determined during the construction of the potential, by fitting to a large database of DFT ‘training’ points (index t), and afterwards kept fixed and tabulated. If we now assume that the α_t are normally distributed, we can determine the so-called *covariance* of two local energies, comparing an LAE from the training data to a new one, and so finding the energy *without* specifically knowing the basis functions themselves. All that is needed to know is an expression for the covariance, also called a *kernel*.

In practice, only a small number of representative, so-called ‘sparse’, points are selected from the entire training database. This choice can be made at random, or using advanced tools such as CUR decomposition [76], which ensures that the selected points are distinct from one another to the greatest degree possible. In the case of NNP, the vast majority of the structures contained in the training database is usually taken into account. While a number of technicalities can be used to e.g. avoid/include unnecessary/representative regions of the configurational space, the sparsity of the data-set does not play a key role in NNPs – as opposed to the GAP framework.

The idea of using neural networks to fit a PES dates back to the 1990s (see e.g. Ref. [55]), whereas a framework capable of dealing with a high-dimensional PES (say, a disordered solid, rather than a single molecule in the gas phase) was introduced in 2007 by Behler and Parrinello [77]. Since then, NNPs have been created for a diverse range of systems, from metal surfaces [78] to water [79].

The GAP framework was introduced in 2010 by Bartók et al., and interatomic potentials for the bulk phases of carbon, silicon and germanium were presented at that time, as well as initial proofs-of-concept for GaAs and iron [80]. Subsequently, Szlachta et al. showed how training databases for GAPs can be constructed in a systematic fashion [81], and such ideas has been a paradigm in MLIP development until today. In that case, fitting a GAP model for tungsten, they started with bulk unit cells and then introduced supercell expansions, point defects, surfaces and dislocations: indeed, the model can ‘learn’ by incorporating additional data [81]. A GAP specifically targeted at an amorphous system was introduced very recently [82], and we will describe this in detail below (Section 4). The GAP code is freely available for non-commercial research at <http://www.libatoms.org>. It consists of two parts: a ‘prediction’ code, which takes parametrised GAP files and uses them to drive simulations (this can be run as a stand-alone program, or via an interface to LAMMPS [83]), and the ‘training’ code which generates a new GAP model from a given set of reference data and input parameters.

It is worth noting that expanding an existing MLIP (for example, from the bulk to surfaces) is usually a one-time investment: once the new DFT reference data have been generated, the potential can be run in a largely similar fashion, and – in the case of GAP – maybe doubles the number of sparse points (with which the speed of the potential scales). A higher price in terms of additional configurations has usually to be paid when extending a NNP to incorporate, e.g. a new phase of the system. Let us say it clearly: MLIPs are *fitting* tools. They can *interpolate* the PES, using the information contained in the reference data-set, but they cannot *extrapolate* to regions of configurational space far outside the database. For example, an MLIP needs to have ‘seen’ surfaces, not just bulk phases, to enable accurate predictions of surface energies [81]. This is often an acceptable price to pay for the largely increased flexibility of the resulting MLIPs.

MLIPs are not limited to inorganic materials, and neither are they limited to DFT, but can be fitted to any suitable quantum-mechanical reference data-set. In the case of GAP, it was shown how high-quality QM data for liquid water can be used to learn for the *error* of DFT with respect to highly accurate correlated quantum-chemistry methods [84]. In turn, this enables predictions at close-to-DFT cost (DFT computations still being required at runtime and forming the ‘core’ of the potential), but approaching the accuracy of the much more advanced QM method. Very recently, a NNP for molecular solids was proposed, giving access to a wide range of different materials built from organic molecules (containing carbon, hydrogen, oxygen and nitrogen) [85].

2.2. What are the limits?

ML-based Interatomic Potentials enable large-scale molecular simulations with quasi-*ab initio* accuracy. This outstanding capability comes at a price, though; namely the sheer computational effort that is usually needed to build (and to expand) the reference data-set. As an example, a NNP recently used to investigate the crystallisation kinetics of GeTe nanowires are based on a data-set of about 45,000 configurations – that is,

45,000 DFT calculations were performed to obtain a reliable NNP [86]. This is perhaps an extreme scenario, in that the above-mentioned NNP can deal with bulk phases as well as surfaces and nanostructures – requiring a huge number of configurations to sample the vast configuration space. However, it is safe to say that the most time-consuming part in the creation of an MLIP is the creation of the data set.

Furthermore, a number of technical issues arise with the fitting procedure itself. As a rule, the more complex the system (that is, the more diverse and extended the LAE), the more these issues become important. However, we shall see in Section 4 that even a supposedly simple disordered system, such as amorphous carbon, can display a diverse variety of structural features, which lead in turn to a complex interplay between the contribution of the different vibrons (e.g. propagons and diffusons, see Figure 1(b)) to the thermal properties of the material. Here follows a non-comprehensive list of the limitations of MLIPs to date:

- **Extrapolation:** As discussed in Section 2.1, MLIPs cannot extrapolate the PES for regions of configurational space that are not represented in the data-set at all.
- **Sparse data-sets:** numerically speaking, it is not easy to produce a MLIP starting from a very sparse data set, i.e. a data-set containing configurations, say bulk cells next to surfaces, whose structures and energies differ strongly. This calls for special measures to be put in place, and is the subject of much of the ongoing research aimed at improving MLIPs.
- **Long-range interactions:** As discussed in Section 2.1, taking into account, e.g. dispersion interactions requires special care.
- **Chemical complexity:** Multicomponent systems, such as ternary or even higher alloys and compounds, are difficult to describe with MLIPs. This is because the number of LAEs increases with the number of components (and drastically so with each added species), and with the increasing difficulty to map a specific LAE onto its energy.
- **The accuracy of the underlying reference data:** MLIPs are normally fitted to DFT energies and forces, aiming to reproduce them as closely as possible, and often tacitly assuming that the reference data are correct. There are, however, several instances where simple density-functional approximations fail [87–89], and then likewise the MLIP must fail – observing *better* agreement with experiment than the DFT result will be merely a fortuitous coincidence. In the future, we expect that this can be partially alleviated by fitting to higher-level DFT or even wavefunction-based data, as already exemplified for water at the CCSD(T) level [84].

In light of these limitations, it is thus our (very personal) opinion that the construction of a MLIP should only be pursued if:

- (1) No other options are available. In many cases, empirical force fields do allow fairly reliable calculations of thermal properties, and nowadays *ab initio* MD can deal with up to 500 particles for up to 1–2 ns;
- (2) The resulting MLIP would allow the investigation of a diverse array of functional (mechanical, thermal,

dynamical...) properties – and thus to pay off in the long run, as opposed to a one-off study. Indeed, considering the cost of creating the reference data-set, the construction of an MLIP is a substantial investment. Several months are typically needed to ‘learn’ crystalline elemental solids, and building an MLIP for the whole phase diagram of a molecular system (such as water) can require several years. A scenario where the construction of MLIPs did pay off is that of the phase-change material GeTe, which will be discussed in the next section.

3. Thermal properties of phase-change materials

The term ‘phase-change material’ (PCM) can, annoyingly enough, refer to two entirely different classes of systems and applications: PCMs for *energy storage* (compounds with a high enthalpy of fusion, used to store energy as latent heat) [90,91], and PCMs for *data storage* [92–94]. The latter, and only the latter, are the topic of this review. They are typically chalcogenide alloys, with compositions along the quasi-binary tie-line that connects the two binary prototype systems GeTe and Sb₂Te₃. The amorphous and crystalline phases of these compounds display a sharp contrast in terms of both optical reflectivity and electrical resistance, and can thus be used to store binary bits of information, zeroes and ones, as structural states of the material. Moreover, the phase transition between the amorphous and crystalline phases (and vice versa) takes place in a matter of nanoseconds, and it is perfectly reversible up to millions of cycles. As such, PCMs are widely considered as very promising candidates for the next generation of non-volatile memories. Excellent review articles about PCMs in general can be found, e.g. in Refs. [28–30]; their computational treatment has been discussed in Refs. [95,96].

The thermal properties of these systems are of key importance for devices. As illustrated in Figure 2, both the *reset* and *set* processes (writing zeroes and ones, respectively) are induced by heating, using laser pulses in optical media and voltage-induced Joule heating in electronic memories. In addition, thermal cross-talk between different regions is detrimental for device performance (and limits data density); it is strongly dependent on the thermal conductivity (κ) of both the crystalline and the amorphous phases. A low thermal conductivity is thus desirable, not only to avoid such cross-talk but also to minimise the electrical current needed to induce the *reset* and *set* processes [30].

Luckily enough, the overwhelming majority of PCMs shows very low thermal conductivity (typically, $\kappa < 1 \text{ W m}^{-1} \text{ K}^{-1}$), both in the amorphous and crystalline phases [97,98]. The low value of κ in Ge–Sb–Te crystals is due to strong phonon scattering from randomly distributed point defects [99,100]. For instance, in GeTe, the variable concentration of Ge vacancies is responsible for the large spread of the experimental data reported for its bulk thermal conductivity [100].

Concerning the amorphous phases, it is crucial to determine whether propagating vibrons characterised by long mean-free paths exist – and to what extent. These *propagons* substantially contribute to the thermal conductivity of, say, amorphous silicon [101], and they are usually absent in nano-structures – simply because their mean-free path is larger than the

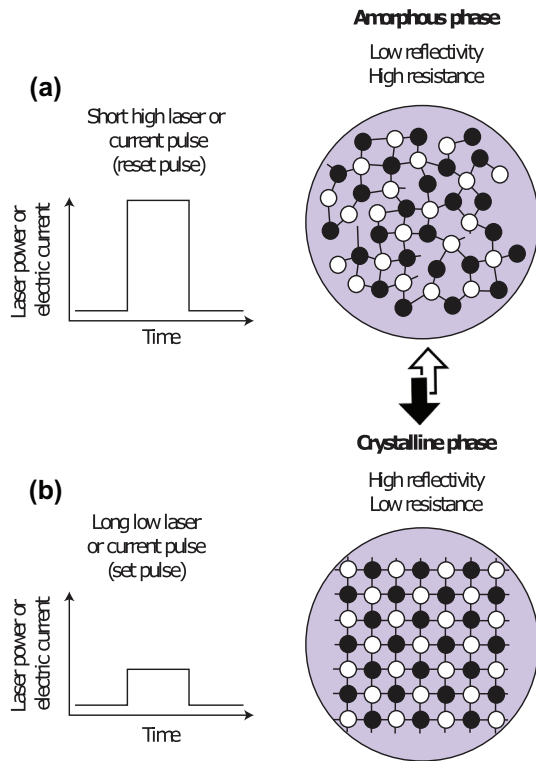


Figure 2. (Colour online) The processes of (a) *reset* and (b) *set* upon which phase change memories are based. In both cases, the active material is heated by either laser or current pulses above its melting temperature. The rapid ($\geq 10^9 \text{Ks}^{-1}$) cooling of such a melt leads to the amorphous phase illustrated in (a). Longer (and less intense) pulses allow for the amorphous phase to crystallise, as depicted in (b). Adapted from Ref. [30]. Copyright 2007 Nature Publishing Group.

dimensionality of the system [102]. As phase-change memories rely on active volumes of the material of the order of a few nanometers only, it is thus important to determine whether the values of κ measured for bulk amorphous GeTe can indeed be used to model the thermal properties of this compound in nano-scaled devices.

Despite its seemingly simple chemical composition, amorphous GeTe displays an intriguing coexistence of tetrahedral and defective octahedral LAO [103–105] (illustrated in Figure 3(c)), extended defects such as chains of homopolar Ge–Ge bonds [106], and nano-voids [107,108]; all of these introduce significant challenges for materials modelling and normally requires a description at the *ab initio* level. While the *vibrational* properties of this system can be indeed described by *ab initio* simulations in small structural models (up to ~ 500 atoms) [104,109], a reliable description of macroscopic *thermal* properties requires much larger systems (containing 10^3 – 10^4 atoms) and longer simulation times (fractions of ns). This is necessary to take into account the above-mentioned disorder and diversity in local environments, and to enable thermal-conductivity calculations both by equilibrium and non-equilibrium MD – as we shall see in the next sections.

A sizable body of experimental work has been devoted to the thermal properties of PCMs (see, e.g. Refs. [110–113]). In terms of simulations, calculations of κ for a few crystalline phases can be found in the recent literature [100,114]. Concerning the amorphous phases, however, the only comprehensive study to date is about GeTe, chiefly because a MLIP for this compound

has been constructed in 2012 [115]. This MLIP belongs to the family of NNPs, and takes advantage of the approach of Behler and Parrinello [77]. Originally developed for the bulk phases (liquid, crystalline, amorphous) of GeTe, the potential has been recently extended to take into account free surfaces and nanostructures [86]. It allows to perform massively parallel MD simulations: good scaling up to 512 cores can be achieved for systems containing $\sim 10^4$ atoms, which in turn can be simulated for as long as several nanoseconds. A number of applications enabled by this potential have been reported, addressing crystallisation kinetics [116] or dynamical properties of the supercooled liquid [106,117], for example. This NNP has been extensively validated in terms of structural and, most importantly here, vibrational properties compared with DFT calculations [115]. Figure 3(a) compares the VDOS for a 4096-atom model of amorphous GeTe with DFT data for a much smaller (216-atom) model. The agreement is remarkable, especially considered that the different contributions to the total VDOS originating from the different LAO are correctly captured by the NNP. The same holds for the Inverse Participation Ratio (IPR; Figure 3(b)), which quantifies the degree of localisation of each vibron, and is defined as

$$\text{IPR}_j = \frac{\sum_{i=1}^N \left| \frac{\bar{e}(j,i)}{\sqrt{m_i}} \right|^4}{\left(\sum_{i=1}^N \frac{|\bar{e}(j,i)|^2}{m_i} \right)^2}, \quad (3)$$

where $\bar{e}(i, j)$ is the j -th vibron eigenvector for the i -th atom with mass m_i . The value of this IPR thus ranges from $1/N$ (completely delocalised) to unity (localised on a single atom). Note that the high IPR values for $\omega > 200 \text{cm}^{-1}$ are due to vibrons strongly localised on tetrahedral Ge [104] atoms.

3.1. The thermal conductivity of amorphous GeTe: three options

Experimental values for the thermal conductivity (κ) of *a*-GeTe range from 0.2 to 0.4 $\text{Wm}^{-1}\text{K}^{-1}$ [97,119,120]. As for the simulations, we have different options: equilibrium molecular-dynamics (EMD), non-equilibrium molecular-dynamics (NEMD), and the analysis of both diffusons and propagons by means of AF theory and the Boltzmann Transport Equation (BTE), respectively. The computational efficiency of MLIPs has now allowed us to compare the κ values calculated by these different approaches side-by-side. This is a unique opportunity to strengthen the reliability of molecular simulations in investigating thermal properties of amorphous solids. In the following sections, we shall consider each of the three above-mentioned computational options.

The total thermal conductivity in a system is given by

$$\kappa = \kappa_{\text{Lattice}} + \kappa_{\text{Electronic}}, \quad (4)$$

where the lattice thermal conductivity originates from vibrons (both in insulating and metallic systems), and the electronic thermal conductivity is due to free conduction electrons (thus relevant for metallic systems only). Amorphous GeTe displays a pseudo-gap in the electronic density of states [121], and as such the contribution of $\kappa_{\text{Electronic}}$ can reasonably be considered as being negligible. In fact, the calculations of κ we are about

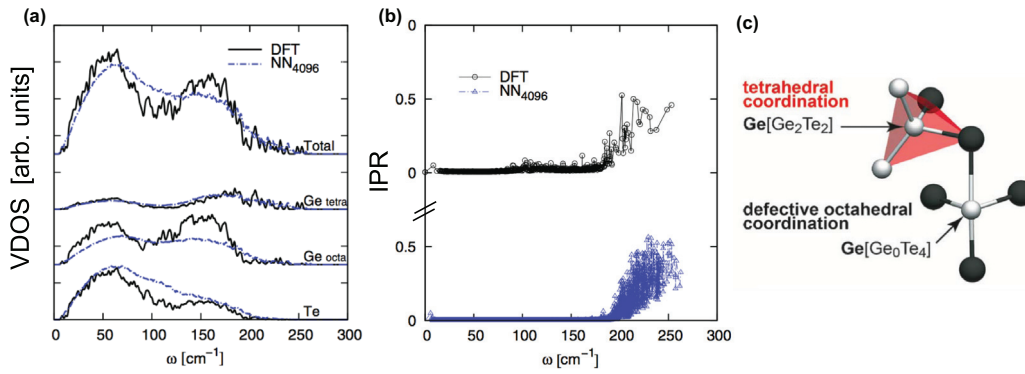


Figure 3. (Colour online) (a) VDOS of a 4096-atom model of amorphous GeTe; both the structure and the vibrational properties were obtained using a NNP. The projections of the total VDOS on different atomic species ($\text{Ge}_{\text{tetra/octa}}$ refer to Ge atoms sitting in tetrahedral and defective octahedral LAEs, see panel (c)) is also reported. The results are compared with those obtained for a smaller (216-atom) model via DFT calculations. (b) Inverse participation ratio (IPR, see text) of phonons (or *vibrons*) in amorphous GeTe. Adapted from Ref. [118]. Copyright 2012 American Physical Society. (c) Coexistence of tetrahedral and defective-octahedral coordination motifs in GeTe. Adapted from Ref. [105]. Copyright 2014 Wiley-VCH.

to discuss refer to κ_{Lattice} only – and we shall see that those account for the whole value of the total κ , confirming the above assumption. It is also worth noticing that κ in principle is a tensorial quantity. This is especially relevant for crystalline systems: for instance, in the well-ordered crystalline phase of $\text{Ge}_2\text{Sb}_2\text{Te}_5$, weak Te–Te bonds along the hexagonal c -axis lead to a strongly anisotropic thermal conductivity [100].

3.1.1. Green–Kubo relation

Transport coefficients, such as κ , can be computed via the so-called Green–Kubo relation from the integrals of specific time-correlation functions. For the thermal conductivity [122],

$$\kappa = \frac{1}{3k_B T^2 \Omega} \sum_{\alpha=1}^3 \int_0^{\infty} \langle \mathcal{J}_{\alpha}(0) \cdot \mathcal{J}_{\alpha}(t') \rangle dt', \quad (5)$$

where Ω , α , and $\mathcal{J}_{\alpha}(t')$ stand for the volume of the simulation box, the α -th Cartesian coordinate and the energy flux, respectively. The latter is also known as the heat flux or the (microscopic) heat current, and it can in turn be written as [122]

$$\mathcal{J}_{\alpha}(t') = \sum_{i=1}^N \epsilon_i(t') \cdot v_{i,\alpha}(t') - \sum_{i=1}^N \sum_{\beta=1}^3 \sigma_{i,\alpha\beta}(t') \cdot v_{i,\beta}(t'), \quad (6)$$

where $\epsilon_i(t')$, $v_{i,\alpha}(t')$ and $\sigma_{i,\alpha\beta}$ are the total energy of the i -th atom, its velocity at time t' , and the element of the atomic stress tensor, respectively. The first term in Equation (6) is commonly referred to as a *convective term*, as it accounts for the heat current originating from atomic motion (convection). It is the main contribution to $\mathcal{J}_{\alpha}(t')$ in gases, important in liquids, but basically negligible for solids, where the self-diffusion is exceedingly low. We thus consider exclusively the second term in Equation (6), which originates from interatomic interactions and it is associated with heat conduction; it is commonly labelled as the *virial term*.

Note that partitioning the total stress into single-particle contributions depends on the particular form of the interatomic potential [123]; in some cases, more than one choice is available. However, in the framework of Behler–Parrinello NNPs, the total

energy of the system is written as a sum of individual atomic energies, so that the definition of an atomic stress follows in a straightforward manner. Note, also, that Green–Kubo relations can be used in *any* equilibrium ensemble, albeit the specific form of $\mathcal{J}_{\alpha}(t')$ is different within different ensembles [122]. Equation (6) refers to the canonical ensemble (‘NVT’).

The time-correlation function in Equation (5) can be obtained by EMD. This is straightforward in principle, and yet substantial statistics are needed to address the tails of the correlation function of the energy flux – and thus to converge the integral in Equation (5). One way to improve numerical accuracy and achieve faster convergence is to rewrite Equation (5) by taking advantage of the Einstein relation [124]:

$$\kappa = \frac{1}{6k_B T^2 \Omega} \lim_{t \rightarrow \infty} \frac{d}{dt} \sum_{i=1}^N \sum_{\alpha=1}^3 \langle [\zeta_{i,\alpha}(t) - \zeta_{i,\alpha}(0)]^2 \rangle, \quad \text{with} \quad (7)$$

$$\zeta_{i,\alpha}(t) - \zeta_{i,\alpha}(0) = \int_0^t \mathcal{J}_{i,\alpha} dt' \quad (8)$$

In the case of α -GeTe, the truncation time t in the integral above was set to 40 ps (Figure 4(a)), and yet 2 ns-long (corresponding in this case to 1,000,000 time steps) simulations were necessary to accumulate sufficient statistics to obtain the value of κ reported in Figure 4(d), which is converged within $0.05 \text{ Wm}^{-1}\text{K}^{-1}$. A number of different methods, such as Homogeneous Non-Equilibrium MD, have been recently proposed to overcome the numerical challenges imposed by the original Green–Kubo approach [127].

3.1.2. Non-equilibrium molecular dynamics

A perhaps more intuitive approach to the calculation of κ is to introduce an actual temperature gradient in the system. Obviously, the resulting simulations would be non-equilibrium ones, but the thermal conductivity can still be evaluated, e.g. via the stationary heat flux density [125–127] from NEMD. For GeTe, Campi *et al.* employed the so-called *reverse NEMD* scheme of Müller–Plathe [128]: a cold and a hot source are placed at the edges of the simulation box, separated by a region of fixed atoms (Figure 4(c)). Note that, as a whole, the simulation box

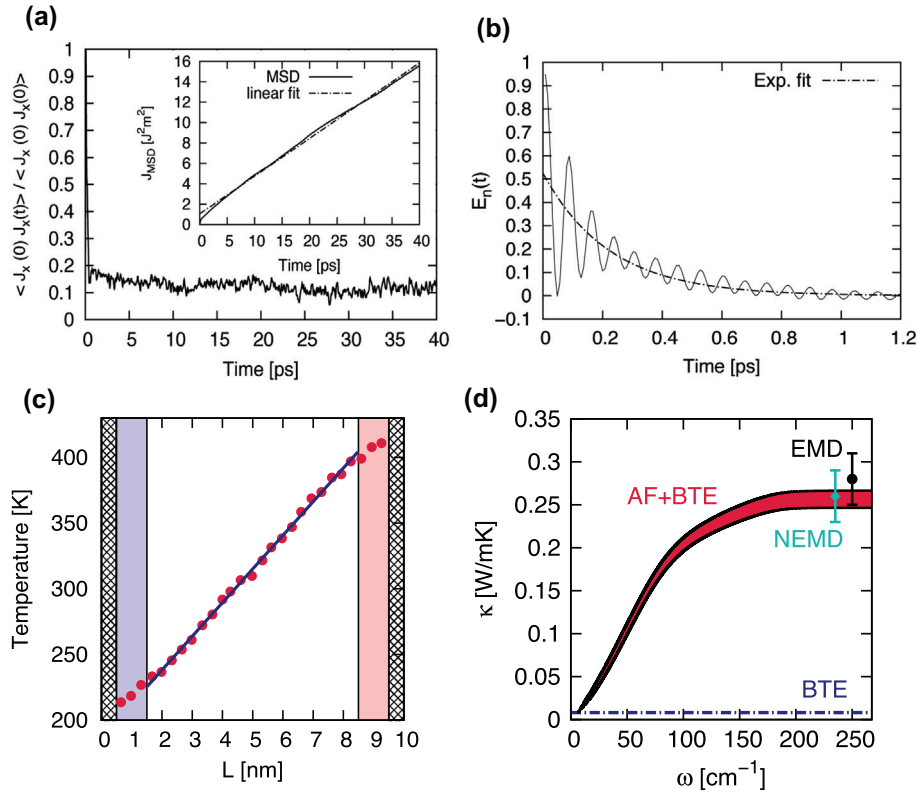


Figure 4. (Colour online) (a) Normalised auto-correlation function of the energy-current operator. The inset shows the MSD of \mathcal{J} according to Equation (8). (b) Decay of the energy of a vibron of a-GeTe at ~ 150 cm⁻¹ as a function of time. Adapted from Ref. [130]. (c) Temperature profile in a reverse NEMD simulation of bulk a-GeTe. Grey, blue and red shaded regions depict the fixed atoms, the cold source and the hot source, respectively. The continuous dark-blue line represents the linear fit of the data. (d) The thermal conductivity κ of amorphous GeTe calculated by means of a NNP using three different approaches. Equilibrium MD simulations taking advantage of the Green-Kubo relation (EMD), non-equilibrium MD simulations using the Müller-Plathe approach (NEMD), and quasi-static calculations (AF+BTE) addressing the contributions of diffusons (according to the Allen-Feldman formalism, AF) and propagons (taken into account by computing the Boltzmann Transport Equation, BTE). In the case of AF+BTE, the reported value of the thermal conductivity for a given frequency ω^* has been obtained by summing the contributions of all phonons characterised by $\omega \leq \omega^*$. Adapted from Ref. [118] - Copyright 2012 American Physical Society.

spans 10 nm (in fact, the largest box considered in Ref. [130] had dimensions: $24.8 \times 24.8 \times 397.3$ Å). This length scale is definitely inaccessible to *ab initio* simulations. Provided that the temperature profile reaches a converged steady-state condition (as illustrated in Figure 4(c)), which for a-GeTe required ~ 800 ps, the bulk thermal conductivity can be computed simply by applying (the one-dimensional) Fourier law [129]:

$$\kappa = -\frac{q_\alpha}{dT/d\alpha}, \quad (9)$$

where q_α is the (imposed) heat flux along the α direction. The value of κ for a-GeTe from these NEMD simulations is 0.26 ± 0.05 Wm⁻¹K⁻¹ [130], in excellent agreement with the outcome of EMD simulations using the Green-Kubo formula (0.27 ± 0.05 Wm⁻¹K⁻¹) [118].

3.1.3. Allen-Feldman theory and the Boltzmann transport equation

The equilibrium (Green-Kubo) and non-equilibrium (Müller-Plathe) MD methods described above take into account all the vibrations of the system: they do not distinguish, say, between localised or extended phonons. As discussed in Section 1, however, different types of phonons contribute to different extents to the vibrational density of states, and thus, to the thermal

conductivity. It would thus be desirable to understand which phonons are responsible for the total value of κ . Recalling the taxonomy illustrated in Figure 1, we have:

$$\kappa_{\text{Total}} = \kappa_{\text{Locons}} + \kappa_{\text{Propagons}} + \kappa_{\text{Diffusons}}. \quad (10)$$

In the case of GeTe, we have not taken into account localised modes (locons). Although such vibrations do populate the high-frequency tail of the VDOS (see Figure 3(b)), their contribution to κ_{Total} is negligible, as will be discussed below. $\kappa_{\text{Propagons}}$ can be obtained by solving the linearised Boltzmann transport equation (BTE) in the single-mode relaxation-time approximation [131]:

$$\kappa_{\text{Propagons}} = \kappa_{\text{BTE}} = \frac{1}{3} \sum_{j=1}^N c_j \cdot v_{g,j}^2 \cdot \tau_j, \quad (11)$$

where c_j , $v_{g,j}$ and τ_j are the specific heat per unit volume, the group velocity and the lifetime of the (harmonic) j -th phonon calculated at the supercell Γ point, respectively. While c_j and $v_{g,j}$ can be straightforwardly calculated from the dispersion curves $\omega_j(q)$ (see, e.g. Ref. [118]), the estimation of the phonon lifetimes τ_j typically requires to converge the following auto-correlation

function:

$$\tau_j = 2 \cdot \int_0^\infty \frac{\langle E_j(t)E_j(0) \rangle}{\langle E_j(0)E_j(0) \rangle}, \quad (12)$$

where $E_j(t) = \frac{1}{N} |\sum_{i=1}^N \sqrt{M_i} \bar{e}_{j,i} \cdot \bar{v}_i(t)|^2$ is the kinetic energy of the j -th mode. Similarly to the auto-correlation function described in Equation (5) in the case of the Green–Kubo approach, long (2 ns) MD trajectories were needed to converge the values of τ_j for a -GeTe, once more highlighting the need for efficient yet accurate MLIPs. It is also worth noticing that, in the case of GeTe, the single-mode relaxation-time approximation of the BTE appears to be valid. In fact, the energy of the phonons does decay following a single exponential relaxation behaviour (Figure 4(b)). Other options to estimate the lifetimes τ_j have been proposed, albeit most of the formulations have been validated for crystalline systems only [132–134].

Perhaps surprisingly, in a -GeTe the overwhelming majority of vibrational modes show a very short mean free path ($\lambda_j = v_{g,j} \cdot \tau_j$), no longer than 10 Å [118]. This is radically different from what has been observed, e.g. in a -Si, where values of λ_j up to 10² Å have been reported [101]. This results in a very low value of $\kappa_{\text{Propagons}}$, viz. 0.01 Wm⁻¹K⁻¹, one order of magnitude smaller than the outcome of both EMD and NEMD simulations.

In fact, $\kappa_{\text{Diffusons}}$ accounts for most of the total thermal conductivity in a -GeTe. Within the theory of AF, each j -th vibron has a *diffusivity* [14,135]:

$$D_{\alpha,j} = \frac{\Omega^2}{8\pi^2 \hbar^2 v_j^2} \sum_{n \neq j} |\langle \bar{e}_j | J_\alpha | \bar{e}_n \rangle|^2 \delta(v_j - v_n), \quad (13)$$

where $\langle \bar{e}_j | J_\alpha | \bar{e}_n \rangle$ are the matrix elements of the α Cartesian component of the energy-flux operator (Equation (6)) between two (harmonic) normal modes \bar{e}_j and \bar{e}_n , with frequencies v_j and v_n , respectively. The resulting contribution to the thermal conductivity is thus frequency-dependent, and it can be written as [14,135]

$$\kappa_{\text{Diffusons}} = \kappa_{\text{AF}} = \sum_{j=1}^N c_j \frac{1}{3} \sum_{\alpha=1}^3 D_{\alpha,j}. \quad (14)$$

As seen in Figure 4(d), $\kappa_{\text{Diffusons}}$ is indeed the major contributor to the thermal conductivity of a -GeTe. This behaviour is in stark contrast with what has been observed, e.g. for a -Si, where propagons also play an important role and indeed $\kappa_{\text{Total}} \approx \frac{1}{2} \kappa_{\text{Propagons}} + \frac{1}{2} \kappa_{\text{Diffusons}}$ [101]. A perhaps simplistic explanation is that a -Si is, compared to a -GeTe, a rather homogeneous system characterised by a relatively low degree of disorder [19, 136–138], so that propagons can actually extend over very long mean-free paths. In contrast, the structure of a -GeTe includes very different local atomic environments as well as nano-cavities and extended defects [103,139]. These structural features scatter and hinder the spatial extent of the propagons, which in turn lead to exceedingly low values of κ_{BTE} for a -GeTe.

At this point, we hope that the reader would be convinced that molecular simulations of vibrational and thermal properties of amorphous solids need to address a number of different, often non-trivial aspects. Assessing which type of vibrons contribute to the thermal conductivity is a good example, as such insight allows to guide experiments and applications. For instance,

in a -GeTe, the absence of spatially extended propagons suggests that the value of κ measured for bulk samples can be safely used to model thermal conductivity at the nanoscale as well – this is of great practical importance for assessing the device performance. On the other hand, the substantial contribution of propagons in a -Si presents the opportunity to tune the thermal conductivity of the material by nanostructuring.

3.2. Thermal boundary resistance at the crystal–amorphous interface

We have discussed in Section 3 the importance of the thermal conductivity for PCM used for non-volatile memories. The latter ultimately rely on the crystallisation/amorphisation of materials such as GeTe, so that the thermal boundary resistance (TBR) between the crystal and the amorphous phase plays a crucial role for device performance. In fact, it is worth investigating the TBR not only at the crystal/amorphous interface, but also at the interfaces between the PCM and the other components of the actual memory cell (dielectrics, such as silicon oxide or silicon nitride, as well as electrode metals such as TiN and Al). In some cases, *ab initio* simulations can be used to study the TBR at the interface between different crystalline phases [100]. However, computing the TBR between the amorphous phase and the crystal does, once more, require the help of MLIPs.

As an example, in Ref. [130], the TBR between crystalline and amorphous GeTe has been calculated by a combination of *ab initio* and classical simulations, the latter taking advantage of the NNP for GeTe discussed above. In this case, the crystal/amorphous interface is a metal/non-metal junction, as the electrical conductivity of crystalline GeTe is much larger (by about three orders of magnitude) than that of the amorphous phase [100]. As such, heat is carried by electrons and phonons alike in the crystal, but only by phonons in the amorphous phase. In addition, while in crystalline GeTe the thermal conductivity originates chiefly from propagons ($\kappa_{\text{Total}} \approx \kappa_{\text{BTE}}$) [100], we have seen in Section 3.1.3 that in a -GeTe $\kappa_{\text{Total}} \approx \kappa_{\text{Diffusons}} \approx \kappa_{\text{AF}}$. A theoretical approach taking this evidence into account has been developed by Majumdar and Reddy [140], and it is based on the following expression for the TBR:

$$\text{TBR}_{\text{Total}} = \text{TBR}_{\text{Lattice}} + \text{TBR}_{\text{Electronic}}, \quad (15)$$

where $\text{TBR}_{\text{Lattice}}$ and $\text{TBR}_{\text{Electronic}}$ are the phononic and electronic contributions to the total TBR. $\text{TBR}_{\text{Electronic}}$ can be written as [140]

$$\text{TBR}_{\text{Electronic}} = \left(\frac{\kappa_{\text{Electronic}}}{\kappa_{\text{Total}}} \right)^{\frac{3}{2}} \cdot (\kappa_{\text{Lattice}} G_{e-ph})^{-\frac{1}{2}}, \quad (16)$$

where the parameter G depends on the electron–phonon coupling constant λ_{e-ph} as well as the electronic density of states at the Fermi level (see, e.g. Ref. [130] for further details). At this stage, it should be quite clear why we need a mixture of *ab initio* and classical simulations to deal with TBR: the calculation of the electron–phonon coupling constant lies within the remit of *ab initio* (DFT) simulations only, whereas large simulation boxes and long simulation times are needed to extract $\text{TBR}_{\text{Lattice}}$

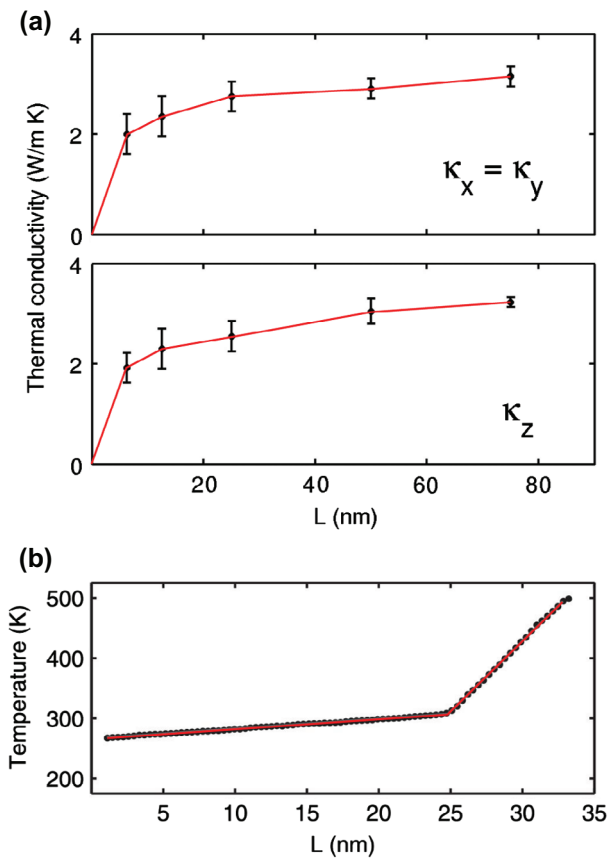


Figure 5. (Colour online) (a) Thermal conductivity κ of crystalline (trigonal) GeTe as a function of the length of the simulation cell L (along the direction of the heat flux). The contributions to κ , split into perpendicular and parallel (with respect to the c -axis of the trigonal crystal) components, are reported in the upper and lower panels, respectively. (b) Temperature profile observed in an NEMD simulation of the junction between amorphous and crystalline GeTe. The amorphous/crystalline interface lies (at 25 nm) on the (0001) crystalline plane of the trigonal crystal (hexagonal cell setup). Adapted from Ref. [130]. Copyright 2015 AIP Publishing LLC.

in the framework of, e.g. the NEMD simulations that we have previously discussed.

In the case of GeTe, TBR_{Lattice} has indeed been obtained by means of the same ‘reverse NEMD’ scheme illustrated in Section 3.1.2, with additional complexity originating from the fact that typically more than one crystal/amorphous interfaces exist. Specifically, Campi et al. considered a -GeTe in contact with either the (0001) or the (2110) crystalline plane of the trigonal crystalline phase. Furthermore, in contrast with amorphous (and thus usually isotropic) systems, one can expect different values of the thermal conductivity along different directions: κ is in fact a tensorial quantity of rank two. Given the symmetry of crystalline GeTe, the direction z (xy) perpendicular (parallel) to the trigonal axis [100] is of particular importance. The resulting values of κ_z and $\kappa_x = \kappa_y$ are reported in Figure 5(a). Note that supercells as large as 80 nm were needed to converge the NEMD simulations. The same can be said for the NEMD calculations of the actual TBR, which led to the temperature profile depicted in Figure 4(b): the jump in the temperature profile for $L \approx 25$ nm in Figure 5 corresponds to the location of the junction between the crystalline and the amorphous phases. Interestingly, it turns out that the electronic contribution to the TBR is a function of the concentration of Ge vacancies

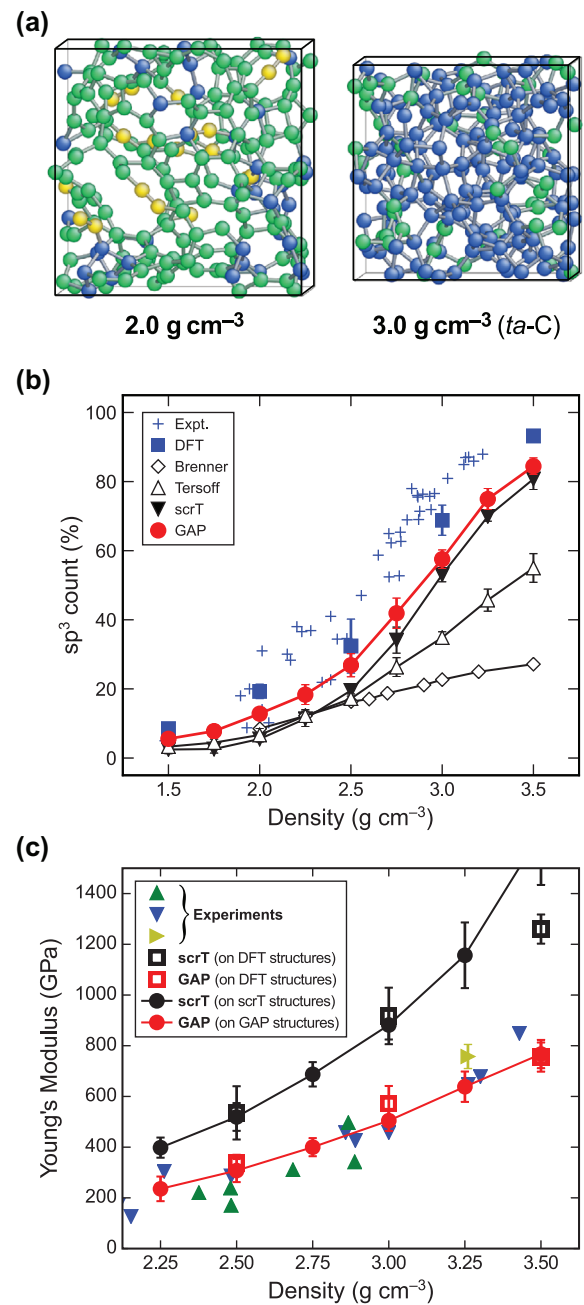


Figure 6. (Colour online) Modelling amorphous carbon and its key properties by ML-based and other simulation methods. (a) Structural models of a -C at 2.0 g cm^{-3} (left) and of ta -C at 3.0 g cm^{-3} (right), generated by quenching from the melt using DFT-MD simulations. In both, the coexistence of sp^2 and sp^3 environments (green and blue, respectively) is apparent; coordination numbers have been determined by counting atomic neighbours up to a 1.85 \AA cutoff. (b) Count of sp^3 atoms, as defined above, as a function of sample density, comparing results from various empirical interatomic potentials, as well as our GAP, to experimental and DFT-based reference data. (c) Same for Young's modulus: coloured symbols indicate experimental data from various references (cf. Ref. [82]); results from our GAP are compared to those of a state-of-the-art empirical interatomic potential. Adapted with permission from Ref. [82]. Copyright 2017 American Physical Society.

that occur in the crystalline phase of GeTe [100]. These defects induce the formation of holes in the valence band, thus affecting the electron–phonon coupling constant. On average, though, $TBR_{\text{Electronic}}$ at the amorphous/crystalline interface is of the same order of magnitude as the TBR_{Lattice} reported for PCMs in contact with metallic systems such as TiN and Al [100].

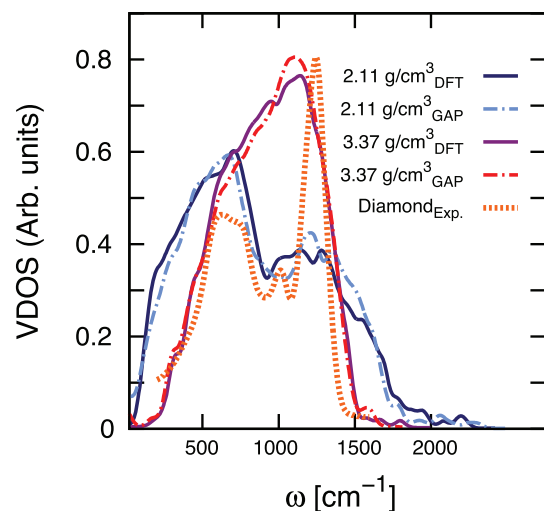


Figure 7. (Colour online) The vibrational density of states (VDOS) of two 216-atom models of amorphous carbon generated as described in Ref. [82] at two different densities: 2.11 and 3.37 g/cm³. A comparison between the VDOS computed via GAP (dashed lines) and that obtained by DFT-LDA calculations (solid lines) is reported. The experimental VDOS of polycrystalline diamond (Diamond_{Exp.}), from Ref. [147]) is also shown – the intensity has been rescaled to the maximum value of the GAP VDOS for high-density *a*-C.

The substantial body of work on the vibrational and thermal properties of *a*-GeTe has been made possible by the construction of a dedicated MLIP. We can only hope that this specific example will foster the creation of new generations of MLIPs in the future, thereby enabling the community to tackle ever more complex disordered systems. To substantiate this point, we will now turn to a different but likewise complex material for which an MLIP has been introduced very recently.

4. From structural to vibrational to thermal properties in amorphous carbon

The large structural diversity in allotropes and compounds of carbon goes back to the element’s ability to form very diverse coordination environments: these are conventionally dubbed ‘sp’ (twofold bonded), ‘sp²’ (threefold bonded), and ‘sp³’ (fourfold bonded). In amorphous carbon (*a*-C), the situation is even more challenging, as these fragments readily exist side-by-side. The dense form, so-called *diamond-like* (or tetrahedral) amorphous carbon in fact contains a mixture of sp² and sp³ environments, as depicted in Figure 6(a); at low densities, linear –C≡C– chains become influential. Indeed, sample density is a key determinant for the structures (and thus properties) of amorphous forms of carbon [141]. A recent review, including several computational aspects, is found in Ref. [142].

This large structural diversity makes it very challenging to accurately describe *a*-C in atomistic simulations. While landmark potentials, such as that by Tersoff [143] and Brenner [144], have long been providing useful insight, they may have significant issues such as with the abundance of sp³ configurations or the description of failure processes. Many of these issues have later been remedied, e.g. using an appropriate environment-dependent cutoff [44], but challenges remain.

Recently, some of us have generated a GAP for liquid and amorphous carbon. In this work, we also introduced an improved set of local descriptors that combines the hitherto

employed SOAP with local, two- and three-body terms. This was found to be very useful to stabilise the potential in regions of high interatomic forces: in the liquid phase at 9,000 K, interatomic forces in carbon regularly exceed 10 eV Å⁻¹, whereas in amorphous carbon at room temperature, they are on the order of only a few eV Å⁻¹.

The new *a*-C GAP [82] has been validated in several ways. Figure 6(b)–(c) collect two of the most crucial quality indicators. In the upper panel, we show the sp³ count as a function of sample density. We have further validated the potential using it for crystal-structure searching, in the spirit of Ref. [145], which led to the identification of several hitherto unknown carbon allotropes [146]. In particular, we fitted a version of the potential that had ‘seen’ no crystalline structures whatsoever – this shows that the PES is trained sufficiently well from liquid and amorphous snapshots to perform *ab initio* random structure searching (AIRSS)-like procedures [145].

We here argue that ML-based potentials will likewise be very useful tools for studying thermal properties of *a*-C. While our work on this is still ongoing, we exemplify this here using a computation of the VDOS and their localisation properties for tetrahedral amorphous carbon (*ta*-C), which we validate against reference DFT computations. The results are reported in Figure 7, where we show the comparison between the VDOS calculated by GAP and that obtained via DFT-LDA calculations – for two 216-atom models of amorphous carbon generated via GAP at two different densities. The agreement between GAP and DFT results is quite encouraging. Importantly, the GAP manages to capture the substantial differences in the VDOS that we observe at low and high density. It is instructive to compare these results with the experimental VDOS of polycrystalline diamond, also reported in Figure 7. The main feature of the VDOS (at ≈ 1250 cm⁻¹) is due to *ideal* sp³ tetrahedral carbon atoms. It can be seen that the – much broader – VDOS of our model of high-density (3.37 g/cm³) *a*-C also peaks at a similar wavenumber. The – even broader – VDOS of our model of low-density (2.11 g/cm³) *a*-C displays its mean peak at lower frequencies (≈ 750 cm⁻¹), while the feature corresponding to sp³ carbon is weaker. This is consistent with the fact that low-density *a*-C contains a much higher fraction of sp² (and, if rapidly quenched from the melt, even of close-to-linear sp) atoms, which lead to vibrational modes characterised by lower frequencies compared to that of sp³ carbon. Conversely, the vast majority of atoms in high-density *a*-C are sp³ hybridized, and lead to a VDOS quite similar to that of polycrystalline diamond.

A full characterisation of the vibrational properties of amorphous carbon at different densities, with special emphasis on the structural features underlying the shape of the VDOS, will be the subject of future work.

5. Conclusions

Our understanding of the thermal properties of amorphous solids has a direct impact on countless practical applications, from optical fibres to digital memories. In principle, molecular simulations could provide valuable insight into the microscopic origin of functional properties, such as thermal conductivity and thermal boundary resistance. However, the absence of long-range order in amorphous solids requires simulation time and

length scales far beyond the reach of *ab initio* methods. Conversely, more often than not, simple classical force fields are not able to describe the structural complexity of these amorphous materials.

Machine Learning-based Interatomic Potentials (MLIPs) offer a way to overcome this standoff, as they allow to perform simulations almost as fast as classical MD – while retaining an accuracy typical of first-principles simulations. The field of MLIPs is developing at a fantastic rate: we have briefly reviewed Neural Network Potentials (NNPs) and Gaussian Approximation Potentials (GAPs), but a number of interesting alternatives are emerging as well. Given the huge momentum presently driving the field of machine learning as a whole, it is reasonable to foresee a rapid expansion of MLIPs for molecular simulations in the very near future.

In this article, we reviewed the body of work that has been devoted to the vibrational and thermal properties of GeTe, a prototype phase-change material for non-volatile data storage. A NNP for this system was built in 2012, and more recently expanded from the crystalline, liquid and amorphous bulk to free surfaces and low-dimensional nanostructures. This potential allowed to quantify the thermal conductivity of amorphous GeTe, and to pinpoint its microscopic origin. The thermal boundary resistance across the interface between the amorphous and crystalline phases has also been calculated, and it is worth noting that the MLIPs for GeTe allowed for the cross-validation of several results obtained by completely different simulation methods – something exceedingly difficult to achieve by means of *ab initio* simulations.

We also explored the capabilities of a GAP recently built to study amorphous carbon, which is widely used in the form of thin films for coatings. This system is especially interesting in that it displays substantial structural differences according to different densities. How does this affect the vibrational and thus the thermal properties? To lay the groundwork for exploring this question, we have here reviewed extensive validation against *ab initio* simulations, and presented the results of a preliminary investigation of the vibrational properties as a function of density. The latter suggests that the heat-conduction mechanism in the two phases could be substantially different, and calls for simulations on a much larger scale which are going to be the subject of future work.

The NNP for GeTe and the GAP for amorphous carbon we discussed here offer unique insight into the thermal properties of these disordered solids. Broadly speaking, we believe that MLIPs provide the opportunity to understand the microscopic origin of functional properties such as thermal conductivity and thermal boundary resistance. This knowledge can aid the design of novel amorphous systems with unique thermal properties, and contribute to bridge the gap between continuous models for thermal transport and molecular simulations. We feel there is enormous potential for the field – even more so as GAP and other frameworks are now publicly available, thus providing the community with the tools of the trade.

The most pressing challenge for MLIPs in the context of thermal properties is perhaps that of addressing the interfaces between different materials, as well as industrially relevant materials such as ceramic matrix composites. The huge configurational space, together with the intrinsic complexity of surfaces

and interfaces call for further improvements to the existing MLIP implementations. In this respect, we hope that this work will encourage the community to take advantage of the capabilities of MLIPs so as to establish molecular simulations as the method of choice to complement and guide the experimental characterisation of the thermal properties of amorphous solids.

Disclosure statement

No potential conflict of interest was reported by the authors.

Funding

G.C.S. is grateful to the Centre for Scientific Computing at the University of Warwick for providing computational resources. V.L.D. gratefully acknowledges a Feodor Lynen fellowship from the Alexander von Humboldt Foundation, a Leverhulme Early Career Fellowship, and support from the Isaac Newton Trust.

ORCID

Gabriele C. Sosso  <http://orcid.org/0000-0002-6156-7399>
Volker L. Deringer  <http://orcid.org/0000-0001-6873-0278>
Gábor Csányi  <http://orcid.org/0000-0002-8180-2034>

References

- [1] Balandin AA. Thermal properties of graphene and nanostructured carbon materials. *Nat Mater*. 2011 Jul;10:569–581.
- [2] Gotsmann B, Lantz MA. Quantized thermal transport across contacts of rough surfaces. *Nat Mater*. 2012 Oct;12:3460.
- [3] Beekman M, Morelli DT, Nolas GS. Better thermoelectrics through glass-like crystals. *Nat Mater*. 2015 Nov;14:1182–1185.
- [4] Russ B, Glaudell A, Urban JJ, et al. Organic thermoelectric materials for energy harvesting and temperature control. *Nat Rev Mater*. 2016 Aug;1:201650.
- [5] Kwon S, Zheng J, Wingert MC, et al. Unusually high and anisotropic thermal conductivity in amorphous silicon nanostructures. *ACS Nano*. 2017 Mar;11:2470–2476.
- [6] Shanker A, Li C, Kim G-H, et al. High thermal conductivity in electrostatically engineered amorphous polymers. *Sci Adv*. 2017 Jul;3:e1700342.
- [7] Wingert MC, Zheng J, Kwon S, et al. Thermal transport in amorphous materials: a review. *Semicond Sci Technol*. 2016;31(11):113003.
- [8] Cahill DG, Braun PV, Chen G, et al. Nanoscale thermal transport II. *Appl Phys Rev*. 2014 Jan;1:011305.
- [9] Tritt TT. Thermal conductivity: theory, properties, and applications New York (NY). Springer. 2004. DOI:10.1007/b136496
- [10] Dove MT. Introduction to the theory of lattice dynamics. *J Neutron*. 2011;12:123–159.
- [11] Ibach H, Lüth H. Solid-state physics, Berlin: Springer. Berlin Heidelberg. 2009. DOI:10.1007/978-3-540-93804-0
- [12] Soppa D, Kotakoski J, Albe K. Finite-size effects in the phonon density of states of nanostructured germanium: a comparative study of nanoparticles, nanocrystals, nanoglasses, and bulk phases. *Phys Rev B*. 2011 Jun;83:245416.
- [13] Donadio D, Galli G. Temperature dependence of the thermal conductivity of thin silicon nanowires. *Nano Lett*. 2010 Mar;10:847–851.
- [14] Allen PB, Feldman JL, Fabian J, et al. Diffusons, locons and propagons: character of atomic vibrations in amorphous Si. *Philos Mag B*. 1999 Nov;79:1715–1731.
- [15] Taraskin SN, Elliott SR. Ioffe-regel crossover for plane-wave vibrational excitations in vitreous silica. *Phys Rev B*. 2000 May;61:12031–12037.

- [16] Wooten F, Winer K, Weaire D. Computer generation of structural models of amorphous Si and Ge. *Phys Rev Lett*. **1985**;54:1392–1395.
- [17] Würger A, Bodea D. Thermal conductivity by two-level systems in glasses. *Chem Phys*. **2004 Jan**;296:301–306.
- [18] Pérez-Castañeda T, Rodríguez-Tinoco C, Rodríguez-Viejo J, et al. Suppression of tunneling two-level systems in ultrastable glasses of indomethacin. *PNAS*. **2014 Aug**;111:11275–11280.
- [19] Cliffe MJ, Bartók AP, Kerber RN, et al. Structural simplicity as a restraint on the structure of amorphous silicon. *Phys Rev B*. **2017 Jun**;95:224108.
- [20] Mi-tang W, Jin-shu C. Viscosity and thermal expansion of rare earth containing soda-lime-silicate glass. *J Alloys Compd*. **2010 Aug**;504:273–276.
- [21] Baesso ML, Shen J, Snook RD. Time-resolved thermal lens measurement of thermal diffusivity of soda-lime glass. *Chem Phys Lett*. **1992 Sep**;197:255–258.
- [22] Oguma M, Fairbanks CJ, Hasselman DPH. Thermal stress fracture of brittle ceramics by conductive heat transfer in a liquid metal quenching medium. *J Am Ceram Soc*. **1986 Apr**;69:C–87.
- [23] Kang J, Han B. First-principles study on the thermal stability of LiNiO₂ materials coated by amorphous Al₂O₃ with atomic layer thickness. *ACS Appl Mater Interfaces*. **2015 Jun**;7:11599–11603.
- [24] Nitta N, Wu F, Lee JT, et al. Li-ion battery materials: present and future. *Mater Today*. **2015 Jun**;18:252–264.
- [25] Terny S, Frechero M. Study of phosphate polyanion electrodes and their performance with glassy electrolytes: potential application in lithium ion solid-state batteries. In: Tiwari A, Kuralay F, Uzun L. editors. *Advanced electrode materials*. Beverly (MA): John Wiley & Sons; **2016**. p. 255–258.
- [26] Pershina SV, Raskovalov AA, Antonov BD, et al. The transport and thermal properties of glassy LiPO₃/crystalline Al₂O₃ (ZrO₂) composite electrolytes. *Ionics*. **2018 Jan**;24:133–138.
- [27] Rodrigues M-TF, Babu G, Gullapalli H, et al. A materials perspective on Li-ion batteries at extreme temperatures. *Nat Energy*. **2017 Jul**;2:17108.
- [28] Raoux S, Welnic W, Ielmini D. Phase change materials and their application to nonvolatile memories. *Chem Rev*. **2010 Jan**;110:240–267.
- [29] Kolobov AV, Tominaga J, editors. *Chalcogenides: metastability and phase change phenomena*. Berlin: Springer; **2012**.
- [30] Wuttig M, Yamada N. Phase-change materials for rewritable data storage. *Nat Mater*. **2007 Nov**;6:824–832.
- [31] Raoux S, Wuttig M. *Phase change materials: science and applications*. New York (NY): Springer; **2010**.
- [32] Siegert KS, Lange FRL, Sittner ER, et al. Impact of vacancy ordering on thermal transport in crystalline phase-change materials. *Rep Prog Phys*. **2015**;78(1):013001.
- [33] Baroni S, de Gironcoli S, Dal Corso A, et al. Phonons and related crystal properties from density-functional perturbation theory. *Rev Mod Phys*. **2001 Jul**;73:515–562.
- [34] Tuckerman ME, Martyna GJ. Understanding modern molecular dynamics: techniques and applications. *J Phys Chem B*. **2000 Jan**;104:159–178.
- [35] Barnett RN, Cleveland CL, Landman U. Structure and dynamics of a metallic glass: molecular-dynamics simulations. *Phys Rev Lett*. **1985 Nov**;55:2035–2038.
- [36] Ercolessi F, Tosatti E, Parrinello M. Au (100) surface reconstruction. *Phys Rev Lett*. **1986 Aug**;57:719–722.
- [37] Ackland GJ, Thetford R. An improved N-body semi-empirical model for body-centred cubic transition metals. *Philos Mag A*. **1987 Jul**;56:15–30.
- [38] Sutton AP, Chen J. Long-range Finnis-Sinclair potentials. *Philos Mag Lett*. **1990 Mar**;61:139–146.
- [39] Daw MS, Foiles SM, Baskes MI. The embedded-atom method: a review of theory and applications. *Mater Sci Rep*. **1993 Mar**;9:251–310.
- [40] Gulenko A, Chungong LF, Gao J, et al. Atomic structure of Mg-based metallic glasses from molecular dynamics and neutron diffraction. *Phys Chem Chem Phys*. **2017 Mar**;19:8504–8515.
- [41] Tangney P, Scandolo S. An *ab initio* parametrized interatomic force field for silica. *J Chem Phys*. **2002 Oct**;117:8898–8904.
- [42] Soules TF, Gilmer GH, Matthews MJ, et al. Silica molecular dynamic force fields—a practical assessment. *J Non-Cryst Solids*. **2011 Mar**;357:1564–1573.
- [43] Cowen BJ, El MS. On force fields for molecular dynamics simulations of crystalline silica. *Comput Mater Sci*. **2015 Sep**;107:88–101.
- [44] Pastewka L, Pou P, Pérez R, et al. Describing bond-breaking processes by reactive potentials: importance of an environment-dependent interaction range. *Phys Rev B*. **2008 Oct**;78:161402.
- [45] Mjølness E, DeCoste D. Machine learning for science: state of the art and future prospects. *Science*. **2001 Sep**;293:2051–2055.
- [46] Jordan MI, Mitchell TM. Machine learning: trends, perspectives, and prospects. *Science*. **2015 Jul**;349:255–260.
- [47] Biamonte J, Wittek P, Pancotti N, et al. Quantum machine learning. *Nature*. **2017 Sep**;549:195–202.
- [48] Savage N. Machine learning: calculating disease. *Nature*. **2017 Oct**;550:S115–S117.
- [49] Behler J. Perspective: machine learning potentials for atomistic simulations. *J Chem Phys*. **2016 Nov**;145:170901.
- [50] van Roekeghem A, Carrete J, Oses C, et al. High-throughput computation of thermal conductivity of high-temperature solid phases: the case of oxide and fluoride perovskites. *Phys Rev X*. **2016 Dec**;6:041061.
- [51] Gaultoi MW, Oliynyk AO, Mar A, et al. Perspective: web-based machine learning models for real-time screening of thermoelectric materials properties. *APL Mater*. **2016 May**;4:053213.
- [52] Thompson AP, Swiler LP, Trott CR, et al. Spectral neighbor analysis method for automated generation of quantum-accurate interatomic potentials. *J Comput Phys*. **2015 Mar**;285:316–330.
- [53] Balabin RM, Lomakina EI. Support vector machine regression (LS-SVM)—an alternative to artificial neural networks (ANNs) for the analysis of quantum chemistry data? *Phys Chem Chem Phys*. **2011 Jun**;13:11710–11718.
- [54] Bartók AP, Csányi G. Gaussian approximation potentials: a brief tutorial introduction. *Int J Quantum Chem*. **2015 Aug**;115:1051–1057.
- [55] Blank TB, Brown SD, Calhoun AW, et al. Neural network models of potential energy surfaces. *J. Chem. Phys*. **1995 Sep**;103:4129–4137.
- [56] Handley CM, Behler J. Next generation interatomic potentials for condensed systems. *Eur Phys J B*. **2014 Jul**;87:152.
- [57] Rupp M, Tkatchenko A, Müller K-R, et al. Fast and accurate modeling of molecular atomization energies with machine learning. *Phys Rev Lett*. **2012 Jan**;108:058301.
- [58] Manzhos S, Carrington T. A random-sampling high dimensional model representation neural network for building potential energy surfaces. *J Chem Phys*. **2006 Aug**;125:084109.
- [59] Hobday S, Smith R, Belbruno J. Applications of neural networks to fitting interatomic potential functions. *Model Simul Mater Sci Eng*. **1999**;7(3):397.
- [60] Behler J. Neural network potential-energy surfaces in chemistry: a tool for large-scale simulations. *Phys Chem Chem Phys*. **2011 Oct**;13:17930–17955.
- [61] Handley CM, Popelier PLA. Potential energy surfaces fitted by artificial neural networks. *J Phys Chem A*. **2010 Mar**;114:3371–3383.
- [62] Rupp M. Machine learning for quantum mechanics in a nutshell. *Int J Quantum Chem*. **2015 Aug**;115:1058–1073.
- [63] MacLeod N, Benfield M, Culverhouse P. Time to automate identification. *Nature*. **2010 Sep**;467:154–155.
- [64] Schramm S. Computer science: data analysis meets quantum physics. *Nature*. **2017 Oct**;550:550339a.
- [65] Thompson LR. A communal catalogue reveals Earth’s multiscale microbial diversity. *Nature*. **2017 Nov**;24621
- [66] Castelvechi D. Artificial intelligence called in to tackle LHC data deluge. *Nat News*. **2015 Dec**;528:18.
- [67] Silver D, Schrittwieser J, Simonyan K, et al. Mastering the game of Go without human knowledge. *Nature*. **2017 Oct**;550:24270.
- [68] Li Z, Kermodé JR, De Vita A. Molecular dynamics with on-the-fly machine learning of quantum-mechanical forces. *Phys Rev Lett*. **2015 Mar**;114:096405.

- [69] Huan TD, Batra R, Chapman J, et al. A universal strategy for the creation of machine learning-based atomistic force fields. *npj Comput Mater.* **2017 Sep**;3: Article No. 37.
- [70] Podryabinkin EV, Shapeev AV. Active learning of linearly parametrized interatomic potentials. *Comput Mater Sci.* **2017 Dec**;140:171–180.
- [71] Behler J. Atom-centered symmetry functions for constructing high-dimensional neural network potentials. *J Chem Phys.* **2011 Feb**;134:074106.
- [72] Ooi N, Rairkar A, Adams JB. Density functional study of graphite bulk and surface properties. *Carbon.* **2006 Feb**;44:231–242.
- [73] Kganyago KR, Ngoepe PE. Effects of local and gradient-corrected density approximations on the prediction of the intralayer lattice distance c , in graphite and LiC_6 . *Mol Sim.* **1999 Feb**;22:39–49.
- [74] Artrith N, Morawietz T, Behler J. High-dimensional neural-network potentials for multicomponent systems: applications to zinc oxide. *Phys Rev B.* **2011 Apr**;83:153101.
- [75] Bartók AP, Kondor R, Csányi G. On representing chemical environments. *Phys Rev B.* **2013 May**;87:184115.
- [76] Mahoney MW, Drineas P. CUR matrix decompositions for improved data analysis. *PNAS.* **2009 Jan**;106:697–702.
- [77] Behler J, Parrinello M. Generalized neural-network representation of high-dimensional potential-energy surfaces. *Phys Rev Lett.* **2007 Apr**;98:146401.
- [78] Artrith N, Behler J. High-dimensional neural network potentials for metal surfaces: a prototype study for copper. *Phys Rev B.* **2012 Jan**;85:045439.
- [79] Morawietz T, Singraber A, Dellago C, et al. How van der Waals interactions determine the unique properties of water. *PNAS.* **2016 Jul**;113:8368–8373.
- [80] Bartók AP, Payne MC, Kondor R, et al. Gaussian approximation potentials: the accuracy of quantum mechanics, without the electrons. *Phys Rev Lett.* **2010 Apr**;104:136403.
- [81] Szlachta WJ, Bartók AP, Csányi G. Accuracy and transferability of Gaussian approximation potential models for tungsten. *Phys Rev B.* **2014 Sep**;90:104108.
- [82] Deringer VL, Csányi G. Machine learning based interatomic potential for amorphous carbon. *Phys Rev B.* **2017 Mar**;95:094203.
- [83] Plimpton S. Fast parallel algorithms for short-range molecular dynamics. *J Comput Phys.* **1995 Mar**;117:1–19.
- [84] Bartók AP, Gillan MJ, Manby FR, et al. Machine-learning approach for one- and two-body corrections to density functional theory: applications to molecular and condensed water. *Phys Rev B.* **2013 Aug**;88:054104.
- [85] Smith JS, Isayev O, Roitberg AE. ANI-1: an extensible neural network potential with DFT accuracy at force field computational cost. *Chem Sci.* **2017 Feb**;8:3192–3203.
- [86] Gabardi S, Baldi E, Bosoni E, et al. Atomistic simulations of the crystallization and aging of GeTe nanowires. *J Phys Chem C.* **2017 Oct**;121:23827–23838.
- [87] Wang CS, Klein BM, Krakauer H. Theory of magnetic and structural ordering in iron. *Phys Rev Lett.* **1985 Apr**;54:1852–1855.
- [88] Grimme S. Seemingly simple stereoelectronic effects in alkane isomers and the implications for Kohn-Sham density functional theory. *Angew Chem Int Ed.* **2006 Jul**;45:4460–4464.
- [89] George J, Reimann C, Deringer VL, et al. On the DFT ground state of crystalline bromine and iodine. *ChemPhysChem.* **2015 Mar**;16:728–732.
- [90] Oró E, de Gracia A, Castell A, et al. Review on phase change materials (PCMs) for cold thermal energy storage applications. *Appl Energy.* **2012 Nov**;99:513–533.
- [91] Agyenim F, Hewitt N, Eames P, et al. A review of materials, heat transfer and phase change problem formulation for latent heat thermal energy storage systems (LHTESS). *Renewable Sustainable Energy Rev.* **2010 Feb**;14:615–628.
- [92] Lencer D, Salinga M, Grabowski B, et al. A map for phase-change materials. *Nat Mater.* **2008 Nov**;7:2330.
- [93] Wuttig M, Salinga M. Phase-change materials: fast transformers. *Nat Mater.* **2012 Mar**;11:3288.
- [94] Deringer VL, Dronskowski R, Wuttig M. Microscopic complexity in phase-change materials and its role for applications. *Adv Funct Mater.* **2015 Oct**;25:6343.
- [95] Akola J, Jones RO. Amorphous structures of Ge/Sb/Te alloys: density functional simulations. *Phys Stat Solid B.* **2012 Oct**;249:1851.
- [96] Zhang W, Deringer VL, Dronskowski R, et al. Density-functional theory guided advances in phase-change materials and memories. *MRS Bull.* **2015 Oct**;40:856.
- [97] Risk WP, Rettner CT, Raoux S. Thermal conductivities and phase transition temperatures of various phase-change materials measured by the 3ω method. *Appl Phys Lett.* **2009 Mar**;94:101906.
- [98] Matsunaga T, Yamada N, Kojima R, et al. Phase-change materials: vibrational softening upon crystallization and its impact on thermal properties. *Adv Funct Mater.* **2011 Jun**;21:2232–2239.
- [99] Lan R, Endo R, Kuwahara M, et al. Electrical and heat conduction mechanisms of GeTe alloy for phase change memory application. *J Appl Phys.* **2012 Sep**;112:053712.
- [100] Campi D, Paulatto L, Fugallo G, et al. First-principles calculation of lattice thermal conductivity in crystalline phase change materials: GeTe, Sb_2Te_3 , and $\text{Ge}_2\text{Sb}_2\text{Te}_5$. *Phys Rev B.* **2017 Jan**;95:024311.
- [101] He Y, Donadio D, Galli G. Heat transport in amorphous silicon: interplay between morphology and disorder. *Appl Phys Lett.* **2011 Apr**;98:144101.
- [102] He Y, Donadio D, Lee J-H, et al. Thermal transport in nanoporous silicon: interplay between disorder at mesoscopic and atomic scales. *ACS Nano.* **2011 Mar**;5:1839–1844.
- [103] Caravati S, Bernasconi M, Kühne TD, et al. Coexistence of tetrahedral- and octahedral-like sites in amorphous phase change materials. *Appl Phys Lett.* **2007 Oct**;91:171906.
- [104] Mazzarello R, Caravati S, Angioletti-Uberti S, et al. Signature of tetrahedral Ge in the Raman spectrum of amorphous phase-change materials. *Phys Rev Lett.* **2010 Feb**;104:085503.
- [105] Deringer VL, Zhang W, Lumeij M, et al. Bonding nature of local structural fragments in amorphous GeTe. *Angew Chem Int Ed.* **2014 Sep**;53:10817–10820.
- [106] Sosso GC, Colombo J, Behler J, et al. Dynamical heterogeneity in the supercooled liquid state of the phase change material GeTe. *J Phys Chem B.* **2014 Nov**;118:13621–13628.
- [107] Akola J, Larrucea J, Jones RO. Polymorphism in phase-change materials: melt-quenched and as-deposited amorphous structures in $\text{Ge}_2\text{Sb}_2\text{Te}_5$ from density functional calculations. *Phys Rev B.* **2011 Mar**;83:094113.
- [108] Upadhyay M, Abhaya S, Murugavel S, et al. Experimental evidence for presence of voids in phase change memory material. *RSC Adv.* **2013 Dec**;4:3691–3700.
- [109] Sosso GC, Caravati S, Mazzarello R, et al. Raman spectra of cubic and amorphous $\text{Ge}_2\text{Sb}_2\text{Te}_5$ from first principles. *Phys Rev B.* **2011 Apr**;83:134201.
- [110] Fallica R, Varesi E, Fumagalli L, et al. Effect of nitrogen doping on the thermal conductivity of GeTe thin films. *Phys Stat Solid RRL.* **2013 Dec**;7:1107–1111.
- [111] Bosse JL, Timofeeva M, Tovee PD, et al. Nanothermal characterization of amorphous and crystalline phases in chalcogenide thin films with scanning thermal microscopy. *J Appl Phys.* **2014 Oct**;116:134904.
- [112] Park S, Park D, Jeong K, et al. Effect of the thermal conductivity on resistive switching in GeTe and $\text{Ge}_2\text{Sb}_2\text{Te}_5$ nanowires. *ACS Appl Mater Interfaces.* **2015 Oct**;7:21819–21827.
- [113] Kusiak A, Battaglia J-L, Noé P, et al. Thermal conductivity of carbon doped GeTe thin films in amorphous and crystalline state measured by modulated photo thermal radiometry. *J Phys Conf Ser.* **2016**;745(3):032104.
- [114] Bosoni E, Sosso GC, Bernasconi M. Grüneisen parameters and thermal conductivity in the phase change compound GeTe. *J Comput Electron.* **2017 Aug**;16:1–6.
- [115] Sosso GC, Miceli G, Caravati S, et al. Neural network interatomic potential for the phase change material GeTe. *Phys Rev B.* **2012 May**;85:174103.

- [116] Sosso GC, Miceli G, Caravati S, et al. Fast crystallization of the phase change compound GeTe by large-scale molecular dynamics simulations. *J Phys Chem Lett.* **2013 Dec**;4:4241–4246.
- [117] Sosso GC, Behler J, Bernasconi M. Atomic mobility in the overheated amorphous GeTe compound for phase change memories. *Phys Stat Solid A.* **2015 Oct**;92:054201.
- [118] Sosso GC, Donadio D, Caravati S, et al. Thermal transport in phase-change materials from atomistic simulations. *Phys Rev B.* **2012 Sep**;86:104301.
- [119] Fallica R, Battaglia J-L, Cocco S, et al. Thermal and electrical characterization of materials for phase-change memory cells. *J Chem Eng Data.* **2009 Jun**;54:1698–1701.
- [120] Zhang S-N, He J, Zhu T-J, et al. Thermal conductivity and specific heat of bulk amorphous chalcogenides $\text{Ge}_{20}\text{Te}_{80-x}\text{Se}_x$ ($x = 0, 1, 2, 8$). *J Non-Cryst Solids.* **2009 Jan**;355:79–83.
- [121] Gabardi S, Caravati S, Sosso GC, et al. Microscopic origin of resistance drift in the amorphous state of the phase-change compound GeTe. *Phys Rev B.* **2015 Aug**;92:054201.
- [122] McQuarrie D. *Statistical mechanics.* Sausalito (CA): University Science Books; **2000**.
- [123] Schelling PK, Phillpot SR, Keblinski P. Comparison of atomic-level simulation methods for computing thermal conductivity. *Phys Rev B.* **2002 Apr**;65:144306.
- [124] Helfand E. Transport coefficients from dissipation in a canonical ensemble. *Phys Rev.* **1960 Jul**;119:1–9.
- [125] Lussetti E, Terao T, Müller-Plathe F. Nonequilibrium molecular dynamics calculation of the thermal conductivity of amorphous polyamide-6,6. *J Phys Chem B.* **2007 Oct**;111:11516–11523.
- [126] Säskilähti K, Oksanen J, Tulkki J, et al. Vibrational mean free paths and thermal conductivity of amorphous silicon from non-equilibrium molecular dynamics simulations. *AIP Adv.* **2016 Dec**;6:121904.
- [127] Dongre B, Wang T, Madsen GKH. Comparison of the Green-Kubo and homogeneous non-equilibrium molecular dynamics methods for calculating thermal conductivity. *Model Simul Mater Sci Eng.* **2017 May**;25(5):054001.
- [128] Müller-Plathe F. A simple nonequilibrium molecular dynamics method for calculating the thermal conductivity. *J Chem Phys.* **1997 Apr**;106:6082–6085.
- [129] Bird R, Stewart W, Lightfoot E. *Transport phenomena.* New York (NY): Wiley international edition, Wiley; **2007**.
- [130] Campi D, Donadio D, Sosso GC, et al. Electron-phonon interaction and thermal boundary resistance at the crystal-amorphous interface of the phase change compound GeTe. *J Appl Phys.* **2015 Jan**;117:015304.
- [131] McGaughey AJH, Kaviani M. Quantitative validation of the Boltzmann transport equation phonon thermal conductivity model under the single-mode relaxation time approximation. *Phys Rev B.* **2004 Mar**;69:094303.
- [132] Pang JWL, Buyers WJL, Chernatynskiy A, et al. Phonon lifetime investigation of anharmonicity and thermal conductivity of UO_2 by neutron scattering and theory. *Phys Rev Lett.* **2013 Apr**;110:157401.
- [133] Togo A, Chaput L, Tanaka I. Distributions of phonon lifetimes in Brillouin zones. *Phys Rev B.* **2015 Mar**;91:094306.
- [134] Wang Y, Shang S-L, Fang H, et al. "First-principles calculations of lattice dynamics and thermal properties of polar solids," *npj Comput. Mater.* **2016 May**;2:20166.
- [135] Allen PB, Feldman JL. Thermal conductivity of disordered harmonic solids. *Phys Rev B.* **1993 Nov**;48:12581–12588.
- [136] Uda T. Atomic structure of amorphous silicon. *Solid State Commun.* **1987 Nov**;64:837–841.
- [137] Treacy MMJ, Borisenko KB. The local structure of amorphous silicon. *Science.* **2012 Feb**;335:950–953.
- [138] Pedersen A, Pizzagalli L, Jónsson H. Optimal atomic structure of amorphous silicon obtained from density functional theory calculations. *New J Phys.* **2017 Jun**;19(6):063018.
- [139] Boschker JE, Wang R, Calarco R. GeTe: a simple compound blessed with a plethora of properties. *CrystEngComm.* **2017**;19(36):5324–5335.
- [140] Majumdar A, Reddy P. Role of electron-phonon coupling in thermal conductance of metal-nonmetal interfaces. *Appl Phys Lett.* **2004 May**;84:4768–4770.
- [141] Robertson J. Diamond-like amorphous carbon. *Mater Sci Eng R Rep.* **2002 May**;37:129–281.
- [142] Laurila T, Sainio S, Caro MA. Hybrid carbon based nanomaterials for electrochemical detection of biomolecules. *Prog Mater Sci.* **2017 Jul**;88:499–594.
- [143] Tersoff J. Empirical interatomic potential for carbon, with applications to amorphous carbon. *Phys Rev Lett.* **1988 Dec**;261:2879–2882.
- [144] Brenner DW. Empirical potential for hydrocarbons for use in simulating the chemical vapor deposition of diamond films. *Phys Rev B.* **1990 Nov**;42:9458–9471.
- [145] Pickard CJ, Needs RJ. *Ab initio* random structure searching. *J Phys Condens Matter.* **2011 Jan**;23:053201.
- [146] Deringer VL, Csányi G, Proserpio DM. Extracting crystal chemistry from amorphous carbon structures. *ChemPhysChem.* **2017 Apr**;18:873–877.
- [147] Bosak A, Krisch M. Phonon density of states probed by inelastic x-ray scattering. *Phys Rev B.* **2005 Dec**;72:224305.